Techniques for the Retrieval of Aerosol Properties over Land and Ocean Using Multi-angle Imaging

John V. Martonchik, David J. Diner, Ralph Kahn,
Mail Stop **169-237**
Jet Propulsion Laboratory, California Institute of Technology
4800 Oak Grove Drive
Pasadena, CA911 09, USA

Thomas P. Ackerman
Department of Meteorology, Pennsylvania State University
University Park, PA 16802, USA

Michel M. Verstraete, Bernard Pinty,
Space Applications Institute
EC Joint Research Centre,
I-2 1020 Ispra (VA), Italy

Howard R. Gordon
Department of Physics, University of Miami
Coral Gables, FL 33124, USA

Submitted to: *IEEE Transactions on Geoscience and Remote Sensing*
November, 1997

ABSTRACT

Aerosols are believed to play a direct role in the radiation budget of Earth but their net radiative effect is not well established, particularly on regional scales. Whether aerosols heat or cool a given location depends on their composition and column amount and also on the surface albedo, information that is not routinely available, especially over land. Obtaining global information on aerosol and surface radiative characteristics, over both ocean and land, is a task of the Multi-angle Imaging SpectroRadiometer (MISR), an instrument to be launched in 1998 on the EOS-AM1 platform. Three algorithms are described that will be implemented to retrieve aerosol properties globally using MISR data. Because of the large volume of data to be processed on a daily basis, these algorithms rely on look-up tables of atmospheric radiative parameters and predetermined aerosol mixture models to expedite the radiative transfer calculations. Over ocean, the "dark water*' algorithm is used, taking full advantage of the nature of the MISR data. Over land, a choice of algorithms is made, depending on the surface types within a scene - dark water bodies, heavily vegetated areas, or high contrast terrain. The retrieval algorithms are tested on simulated MISR data, computed using realistic aerosol and surface reflectance models. Results of retrieval sensitivity studies to aerosol properties and the Sun-view geometry are presented.

I. INTRODUCTION

Concern about the impact of aerosols on global climate is creating a resurgence of research interest. This is fueled by a number of issues; most notable is the current effort to define the extent and limits of the greenhouse problem. Many recent papers have attempted to link increased anthropogenic activity to increased aerosol production, resulting in decreased insolation, thus mitigating the anticipated rise in global surface air temperature caused by enhanced concentrations of greenhouse gases (e.g., [1]-[3]). However, these studies do not provide a clear and concise solution to the problem. The most recent IPCC report [4] provides a review of the tropospheric aerosol issue and concludes that direct aerosol forcing is on the order of 0.5 W/m^2, uncertain to a factor of two. The impacts of changing particle properties on clouds (aerosol "indirect" effects) are even less well understood.

We can identify at least three reasons for the uncertainty in direct aerosol forcing. These are

(1) the lack of a global climatology of aerosol optical depth, (2) the uncertainty in aerosol composition and associated single-scattering al bedo, and (3) the paucity of knowledge of spatial and temporal variability on (he regional scale. Aerosol column amount (i.e., optical depth) is the fundamental parameter required to understand direct impacts on the solar radiation balance.

Obviously, global climate studies require a global optical depth climatology, but such a database does not currently exist. The most extensive climatology available today uses solar reflectance measured by AVHRR, and has provided coverage of the world's oceans equatorward of 70 ^{0}latitude since 1987 [5]. Although this climatology is very useful and offers some interesting insights into global aerosol processes, it has two major deficiencies. The first is the lack of optical depth values over land. Although oceans cover the bulk of the Earth's surface, land areas are the source of the majority of particles and essentially all anthropogenic production. In general, we expect to find the largest optical depth values over land and coastal ocean. The inability of the AVHRR algorithm to retrieve land optical depths leaves a critical component of the problem unaddressed. Second, the retrieval algorithm assumes a fixed size distribution and index of refraction, which in essence means a fixed phase function. Since the reflected radiation depends on the phase function as well as the optical depth, this produces an unresolvable ambiguity in the retrieval.

A variety of ground-based aerosol optical depth time series are available, but these are limited in spatial coverage. As a result, assessments of the global impacts of aerosol have largely been based on a grossly inadequate knowledge of the optical depth climatology, and practically no knowledge of the scattering phase function or asymmetry factor.

In an effort to meet these observational needs, the Multi-angle Imaging SpectroRadiometer (MISR) instrument, scheduled for launch in 1998 aboard the Earth Observing System-AM 1 platform, is capable of continuously imaging the surface at nine fixed viewing angles (nadir plus 70.5°, 60.0°,45.6°,26.10 forward and aftward of nadir) and four spectral bands (446, 558,672, and 866 nm) [6]. A given scene will be imaged with all 36 combinations of view angle and wavelength nearly simultaneously (within a span of 7 minutes), allowing us to assume that the atmospheric aerosols in the scene remain constant during the course of the measurements. The MISR aerosol retrieval algorithms are designed to exploit the instrument's unique angular coverage to better characterize aerosol properties. The footprint size o! the globally produced MISR data is nominally 1.1 km (termed a subregion), but the aerosol retrieval is actually performed over a 16x 16 array of sub-

regions, i.e., a 17.6 km x 17.6 km area. This lower spatial resolution for aerosol retrievals allows for considerable flexibility in [he way the retrievals arc performed, while still providing useful information on local, regional, and synoptic scales.

II. AEROSOL RETRIEVAL STRATEGY

The retrieval of aerosol properties by remote sensing is a notoriously under-determined problem. The only demonstrated global-scale, satellite-based retrieval of aerosols derives aerosol optical depth from single-angle, monospectral data, using assumed values for all the aerosol microphysical properties. The MISR aerosol retrieval builds upon earlier work, making use of the multi-angle data to remove much of the ambiguity. Our retrieval strategy is based on a few assumptions and other considerations:

1) We assume atmospheric aerosols are homogeneous within a 17.6 km^2 region at the surface, growing to about 75 km^2 in area at an altitude of 10 km. With this assumption, a strength of the multi-angle technique is that the different effective path lengths, observed through the atmosphere, vary in a predictable way.

2) We perform our retrievals by comparing observed radiances with model radiances calculated for a suite of aerosol compositions and size distributions that covers a range of expected natural conditions. This makes the retrieval computationally efficient, and allows us to make use of climatological constraints on aerosol properties and to determine whether the observations are consistent with various climatological expectations.

3) We adopt the χ^2 statistical formalism to assess the magnitude of the residuals in the comparisons, and report all models that meet the acceptance criteria. This approach explicitly includes instrument measurement uncertainty in the retrieval results.

4) The largest uncertainty in the retrieval algorithm is the reflectance of the underlying surface. We have three distinct aerosol algorithms, selectively used with data taken over surfaces with progressively less-well-constrained reflectance properties: dark water, dense dark vegetation (DDV), and heterogeneous land. For dark water, we assume the water-leaving radiance is negligible at red and near-IR wavelengths, and explicitly account for specular reflection and whitecaps. For DDV, wc assume an angular shape for the surface bidirectional reflectance factor (BRF) and

leave the absolute reflectivity as a free parameter, and for heterogeneous land, we do not make any assumptions about the BRF but represent it as a sum of empirical orthogonal functions, derived from the data themselves.

5) We expect to be able to distinguish airmasses holding different types of aerosols. The strength of the MISR aerosol data is its information about the global, temporally varying context; our data is complementary to in situ measurements, and we plan to use them to determine the detailed aerosol properties within air masses wherever possible.

6) Because our retrieval algorithms presently require an assumption of horizontal atmospheric homogeneity, no aerosol retrievals will be performed over land when the surface topography is complex. Additionally, we filter out subregions that are cloud-contaminated or, over water, contaminated by glint.

7) A number of configurable parameters in the algorithms will be adjusted after launch to improve the performance of the algorithms with real MISR data.

A. Aerosol Climatology Product

In order to constrain the MISR aerosol retrievals, it is advantageous to make reasonable use of what is known about the types of aerosols that are found in the troposphere. In general, tropospheric aerosols fall into a small number of compositional categories, which include sea spray, sulfate/nitrate, mineral dust, biomass burning particles, and urban soot. Typical values for approximate size ranges, and the proclivity of each particle type to adsorb water under increasing relative humidity are also available in the literature. Therefore, we completely prescribe the physical and chemical (and therefore optical) properties of candidate aerosols. The one advantage of this approach is that it makes use of what is already known about aerosols to remove some of the ambiguity about aerosol properties in the information content of the MISR measurements. To this end, a review of published aerosol climatologies was performed (including [7]- [10] and many others). Aerosol attributes typical of natural conditions as described in these references (such as compositional and size classes) are adopted in the MISR retrievals. However, other attributes, such as aerosol column amount, aerosol type, and specific spatial and temporal distributions, are left to be determined by [he retrievals.

The aerosol information used by the MISR retrieval algorithms is contained in the Aerosol Climatology Product (ACP) [11] which is composed of three parts: 1) an aerosol physical and optical properties (APOP) file, 2) a tropospheric aerosol mixture file, and 3) an aerosol climatology file. This dataset will reside at the NASA Langley Distributed Active Archive Center (DAAC), where all the MISR data processing is done, and will be available to users of the MISR aerosol products who want additional information about MISR-retrieved aerosols. The APOP file contains the microphysical and scattering characteristics of the individual, single composition, single particle size distribution (so called "pure") aerosol models upon which the retrievals are based. The particle physical properties (size distribution, index of refraction, and tendency to adsorb water) are based upon current climatology data. The effective optical properties are calculated using Mie theory for spherical particles, and ellipsoid approximations/geometric optics for non-spherical cases [12], [13], for a range of relative humidities (RH). Size statistics are calculated, and optical properties are reported for all MISR bands. A list of the APOP pure particle types and some of their attributes is given in Table 1. All aerosols are modeled using a log-normal particle size distribution, except for near-surface fog, which follows a power law, Both types of distributions are characterized by a minimum and maximum radius, r_1 and r_2, respectively. The log-normal distribution is also parametrized by the characteristic radius r_c and characteristic width σ, whereas the power law distribution is parametrized by an exponent a. The effective radius r_{eff} of the distribution is an average over the distribution, weighted by the geometrical cross-sectional area of the particles.

During the retrieval process, mixtures of these pure particles are generated to simulate the more complex aerosol compositions encountered in the troposphere. Table 2 shows the initial suite of mixtures specified in the tropospheric aerosol mixture file of the ACP. The relative abundances, expressed as percentages of the total aerosol extinction optical depth, are wavelength and relative humidity dependent, due to the dependence of extinction cross section on wavelength and RH. The entries in Table 2 are for the MISR green band (558 nm) and 70% RH. Finally, the third file in the ACP provides aerosol climatology information (mixture type, optical depth at 558 nm, and estimated likelihood of occurrence) on a 1° latitude-longitude global grid and in monthly intervals. This file is not used in the aerosol retrieval process, but provides a "post algorithm" mechanism for finding anomalous conditions, which may indicate the discovery of unexpected aerosol types and distributions, or limitations of the algorithms.

B. Simulated MISR Ancillary Radiative Transfer (SMART) Dataset

In addition to predetermined aerosol types, another major feature of the aerosol retrieval strategy is the use of a look-up table instead of real-time calculations to obtain most of the radiative transfer parameters needed by the algorithms. Whether retrieving aerosols over ocean or land, the fundamental process involves comparing measured top-of-atmosphere (TOA) radiances to those derived from an atmosphere/surface radiative transfer (RT) model. To accommodate the timing requirements of analyzing the large amount of observational data obtained on a daily basis and the required modeling of relatively complex radiative transfer processes in the retrieval algorithms, many of the necessary RT parameters required by the algorithms have been precomputed, based on the pure aerosol models contained in the ACP. The results are stored in the Simulated MISR Ancillary Radiative Transfer (SMART) dataset [11]. This dataset contains aerosol-dependent black surface atmospheric path radiances, diffuse transmittances, irradiances, and bihemispherical albedos in addition to the TOA radiance components contributed by a windspeed-dependent ocean surface. Using these parameters, the TOA radiances both over ocean and land, required by the aerosol retrieval algorithms, are then computed for all the aerosol mixture models in the ACP.

Here is a summary of the MISR aerosol retrieval strategy: From the data contained in the ACP and SMART datasets, TOA radiances for mixtures of pure aerosol types are computed and compared with the MISR observations to determine those models that provide good fits to the data. Both aerosol type and optical depth are retrieved in this process. Three retrieval algorithms are available. One is used over dark water and two over land; only one is selected for a given region based on a hierarchical scheme which depends on the surface type (dark water, dense dark vegetation, or heterogeneous land). These three algorithms are schematically illustrated in Figure 1. For a region, defined as 17.6 km x 17.6 km in size, the algorithm determines whether any of the 16x16 subregions can be classified as dark water. If there are any dark water subregions within the region, the “dark water” retrieval algorithm is used. If no dark water subregions are found, a search is made for subregions classified as dense, dark vegetation (DDV). If any are found, the “DDV” retrieval algorithm is used. If no DDV subregions are found, the selection defaults to the “heterogeneous land” algorithm. Regardless of the retrieval path chosen, an aerosol column amount upper bound, based on the darkest radiance observed in the region, is also calculated.

III. MODELING OF TOA RADIANCE

The TOA radiance, L_λ^{TOA}, at wavelength λ can generally be expressed as the sum of two parts,

$$L_\lambda^{TOA}(-\mu, \mu_0, \phi - \phi_0; \tau_\lambda) = L_\lambda^{atm}(-\mu, \mu_0, \phi - \phi_0; \tau_\lambda) + L_\lambda^{surf}(-\mu, \mu_0, \phi - \phi_0; \tau_\lambda), \quad (1)$$

where L_λ^{atm} is the radiance which has been scattered by the atmosphere to space without interacting with the surface (i.e., the path radiance) and L_λ^{surf} is the additional radiance at the top of the atmosphere produced by the interaction of the downward directed atmospheric radiance with the surface. The cosines of the view and solar angles are $-\mu$ and μ_0, respectively, ϕ-ϕ_0 is the view azimuth angle with respect to the solar position, and τ_λ is the total (Rayleigh + aerosol) extinction optical depth.

The aerosol retrieval process requires a determination of the path radiance L_λ^{atm} for aerosol mixtures defined in the ACP. In principle, the most exact way to do this is to perform the appropriate radiative transfer calculations for the aerosol mixture and store the results in the SMART dataset. However, to allow more flexibility in our ability to define mixtures and to minimize the required storage space for the SMART dataset, we use an approximation which requires knowledge of only the optical properties and the computed path radiances of the individual components making up the aerosol mixture. This approximation, described by Abdou et *al. [15],* is a modification of the standard linear mixing approach, e.g., [14], and provides a much more accurate calculation of L_λ^{atm} than standard linear mixing in situations where particles with substantially different absorption characteristics are present. Application of modified linear mixing to the path radiance has been tested for all combinations of aerosols contained in the ACP, and provides sufficiently accurate results for all mixture cases in Table 2 up to total aerosol optical depths of at least 2. There is minimal computation for L_λ^{atm}, since all the necessary optical parameters are obtained from the ACP while the component path radiances are obtained from the SMART dataset, stored as functions of $-\mu, \mu_0, \phi$-ϕ_0, and τ_λ.

The surface contribution L_λ^{surf} to the TOA radiance in (1) can be written as

$$L_\lambda^{surf}(-\mu, \mu_0, \phi - \phi_0; \tau_\lambda) = \exp(-\tau_\lambda/\mu) \cdot \frac{1}{\pi} \int_0^{2\pi} \int_0^1 R_\lambda^{surf}(-\mu, \mu', \phi - \phi') L_\lambda^{inc}(\mu', \mu_0, \phi' - \phi_0; \tau_\lambda) \mu' d\mu' d\phi'$$

$$+ \frac{1}{\pi} \int_0^{2\pi} \int_0^1 \int_0^{2\pi} \int_0^1 T_\lambda(-\mu, -p'', \phi - \phi''; \tau_\lambda) R_\lambda^{surf}(-\mu'', \mu', \phi'' - \phi') L_\lambda^{inc}(\mu', \mu_0, \phi' - \phi_0; \tau_\lambda) \mu' d\mu'' d\phi'' d\mu' d\phi' \quad (2)$$

where L_λ^{inc} is the incident radiance at the surface, T_λ is the upward diffuse transmittance. and R_λ^{surf} is the surface BRF. The treatment of this component varies among our three aerosol retrieval techniques and, therefore, will be discussed on an individual basis.

IV. AEROSOL RETRIEVAL OVER DARK WATER

Because the reflectance of large water bodies (e.g., the ocean) is often uniform, and deep water bodies have negligible water-leaving radiance at red and near-infrared wavelengths, considerable progress has been made in development of algorithms to retrieve aerosol properties over dark water. By assuming an aerosol model (i.e., specification of a particular mixture), it is possible using radiative transfer theory to derive a one-to-one relationship between observed radiance and aerosol column amount. Such modeling has been applied to the retrieval of aerosol concentration from Landsat [16], [17] and NOAA AVHRR [18]-[21], [5] single-view radiances. Multi-angle radiances, which are governed strongly by the shape of the aerosol scattering phase function, provide additional information with which to refine the aerosol model used in the retrieval of optical depth.

A. Surface Contribution to TOA Radiance

The ocean surface BRF, R_λ^{surf}, in (2) is computed using the Kirchhoff approach to modeling the radiance scattered from a randomly rough surface [22], [23]. The rough surface is modeled as an isotropic, Gaussian distribution of surface slopes with a dependence on surface windspeed w_{surf}, based on the empirical formula of Cox and Munk [24] and includes wave shadowing effects. Empirical estimation of whitecap reflectance [25], [26] is also included in the BRF model. Once R_λ^{surf} *is* determined, the surface contribution L_λ^{surf} for a particular atmospheric model can be directly computed from (2).

The surface contribution for an aerosol mixture is obtained using standard linear mixing. Standard linear mixing is adequate here because L_λ^{surf} is dominated by the properties of the surface

13 RF. Like the atmospheric path radiance, [he surface contributions for the individual components of the aerosol mixture are obtained from the SMART dataset, stored as functions of $-\mu, \mu_0, \phi-\phi_0, \tau_\lambda$ and w_{surf} [1 1]. For operational data processing at the DAAC, estimates of the surface windspeed are obtained from the EOS Data Assimilation Office (DAO).

B. Criteria for Aerosol Best Estimate

For a specified surface windspeed and view/solar geometry corresponding to a particular measurement, the TOA radiances in the red (672 nm) and near IR (866 nm) MISR bands are determined at each camera angle for each aerosol mixture model to be tested. The retrieval is based on a comparison of the radiances for each model and aerosol column amount with the actual MISR observations, using several types of residuals as test variables. A single retrieval is performed over a 17.6 km x 17.6 km region, using the median values of the MISR radiances from all cloud-free subregions within the region. For this retrieval algorithm and the two that are used over land, it is assumed that the atmospheric properties, i.e., path radiances and transmittances, do not vary over a region.

The criterion used to find the best-fitting aerosol model is minimization of the χ^2_{abs} test variable, calculated as a function of aerosol column amount (described by the optical depth at 558 nm, τ_{558})]

$$\chi^2_{abs}(\tau_{558}) = \frac{\sum_{\lambda}\sum_{j} w_{\lambda j} \cdot \dfrac{[L_\lambda^{MISR}(j) - L_\lambda^{TOA}(j;\tau_\lambda)]^2}{\sigma^2_{abs,\lambda}(j)}}{\sum_{\lambda}\sum_{j} w_{\lambda j}}, \qquad (3)$$

where the argument j is shorthand for the camera geometry, $(\mu_j, \mu_0, \phi_j - \phi_0)$ of the jth camera, L_λ^{MISR} is the median MISR radiance, L_λ^{TOA} is the model TOA radiance for the aerosol mixture, and $\sigma_{abs,\lambda}$ is the absolute radiometric uncertainty in L_λ^{MISR} [27]. The sum in j is over the nine MISR cameras and the sum in λ is over the two bands at 672 and 866 nm, the wavelengths at which [he dark water surface is assumed to have negligible water-leaving radiance. For a valid value of L_λ^{MISR} in the jth camera the weight $w_{\lambda j}$ is equal to the inverse of the cosine of the view angle of camera j, providing a greater weighting of the more oblique cameras to take advantage of the longer atmospheric slant path. When the value of L_λ^{MISR} m the jth camera is not valid (e.g., due to cloud

contamination or channel failure) then w_{λ_j} is set equal to zero.

For each candidate model we evaluate χ^2_{abs} over a range of aerosol column amount and determine the minimum χ^2_{abs} and its corresponding optical depth, $\tau_{558}^{bestfit}$. This minimum is determined by fitting a parabolic curve through the smallest computed χ^2_{abs} and its two neighboring values on the τ_{558} grid,

$$\ln\left[\chi^2_{abs}(\tau^2_{558})\right] = A + B\tau_{558} + C\tau^2_{558}. \tag{4}$$

The logarithm of χ^2_{abs} is used instead of χ^2_{abs} to guarantee that the minimum value, $\chi^2_{abs,\,min}$, determined from the fitting procedure, is always positive. Then the optical depth at this minimum is given by

$$\tau_{558}^{bestfit} = \frac{-B}{2C} \tag{5}$$

with an uncertainty

$$\Delta\tau_{558}^{bestfit} = \sqrt{\frac{\ln\left(1 + \frac{1}{\chi_{abs,\,min}}\right)}{C}}. \tag{6}$$

This uncertainty is defined as the optical depth difference from $\tau_{558}^{bestfit}$ needed to increase $\chi^2_{abs,\,min}$ by 1.

‘rice $\chi^2_{abs,\,min}$ has been found, its value establishes whether the candidate aerosol model provides a good fit to the measurements. A value of $\chi^2_{abs\,min} \leq 1$ indicates a good fit but, to allow for unmodeled sources of uncertainty, we establish $\chi^2_{abs\,min} \leq 2$ as an acceptable fit. Since there are 18 measurements (nine angles and two spectral bands) for each ocean retrieval, there is more than one piece of information we can use in comparing the model with the observations. Thus, we define other test variables to help determine the goodness of fit of the particular aerosol model to the MISR data. These additional parameters are calculated for the aerosol optical depth, $\tau_{558}^{bestfit}$. One of these goodness-of-fit test variables, χ^2_{geom}, is a comparison of the angular shape normalized to a reference camera (nominally the nadir view camera), which emphasizes camera-to-camera geometric differences,

$$\chi^2_{geom}(\tau_{558}^{bestfit}) = \frac{\sum_{\lambda}\sum_{j} w_{\lambda j} \cdot \dfrac{\left(\dfrac{L_\lambda^{MISR}(j) \quad L_\lambda^{TOA}(j;\tau_\lambda^{bestfit})}{L_\lambda^{MISR}(ref) \quad L_\lambda^{TOA}(ref;\tau_\lambda^{bestfit})} \right)^2}{\sigma^2_{geom,\lambda}(j, ref)}}{\sum_{\lambda}\sum_{j} w_{\lambda j}}. \tag{7}$$

The argument *ref* is shorthand for the reference camera geometry, $(\mu_{ref}, \mu_0, \phi_{ref} - \phi_0)$ and $\sigma_{geom,\lambda}$ is the uncertainty in the measured camera-to-camera radiance ratio [27]. Another goodness-of-fit test variable, χ^2_{spec}, is a comparison of the spectral ratio relative to the red band,

$$\chi^2_{spec}(\tau_{558}^{bestfit}) = \frac{\sum_{j} w_j \dfrac{\left(\dfrac{L_{866}^{MISR}(j)}{L_{672}^{MISR}(j)} \Big/ \dfrac{L_{866}^{TOA}(j;\tau_{866}^{bestfit})}{L_{672}^{TOA}(j;\tau_{672}^{bestfit})} \right)^2}{\sigma^2_{spec}(j)}}{\sum_{j} w_j}, \tag{8}$$

where σ_{spec} is the uncertainty in the measured band-to-band radiance ratio [27].

The metrics given in (7) and (8) take advantage of the smaller instrument relative uncertainties as compared to the absolute uncertainty, thus providing potentially greater sensitivity. Simulations have shown that χ^2_{geom} tends to be more sensitive to particle size than to composition, whereas χ^2_{spec} tends to depend more on both particle size and composition.

Finally, we define a maximum deviation test variable,

$$\chi^2_{maxdev}(\tau_{558}^{bestfit}) = \underset{\lambda,\, j}{Max}\left\{ \frac{[L_\lambda^{MISR}(j) - L_\lambda^{TOA}(j;\tau_\lambda^{bestfit})]^2}{\sigma^2_{abs,\lambda}(j)} \right\}, \tag{9}$$

to find the camera and band at which the observed radiance is most different from the model radiance. This test variable is effective at picking out optical features such as “rainbows”.

Successful aerosol models are those for which all four metrics, χ^2_{abs}, χ^2_{geom}, χ^2_{spec}, and $\chi^2_{\text{fills.tdt'b,}}$ fall below threshold values. These threshold values are nominally set to 2 for all four but may be adjusted pending further theoretical sensitivity studies and experience with actual MISR

data.

The radiometric performance of the instrument will dictate which aerosol models fit the data to within the instrumental uncertainties. Any model which meets the criteria described above is deemed a valid fit. Of course, the best situation is that only one of the many aerosol mixtures tested will qualify as satisfactory. However, it is possible for more than one model to satisfy the goodness-of-fit criteria. Resolution of such ambiguities, which is not part of the DAAC operational aerosol retrieval process, will require reference to additional information, such as the climatological likelihood parameters contained in the Aerosol Climatology Product. It is also possible that no model will qualify as fitting the observational data. This may be indicative of a failure of the predetermined models to represent the ambient atmospheric state, or some limitation of the algorithm or instrument performance. Experience with actual MISR data will be necessary to determine if any aerosol models need improvements. In any event, information on the fits for all aerosol models tried in the retrieval will be logged as part of the MISR Aerosol Product. An Aerosol Retrieval Success Indicator is established for each region as a simple way of determining (e.g., for subsequent surface retrieval processing) if at least one good fitting model has been found. Assuming that at least one model meets the goodness-of-fit criteria, two overall best estimates of aerosol column amount are also calculated, the mean and the median of the individual successful model amounts.

C. Aerosol Retrieval Simulations

To test MISR'S sensitivity to aerosol properties over dark water, we simulated MISR data, using aerosol models in which column amount, particle size, and the real and imaginary index of refraction were varied over a wide range of values. We designated one set of MISR TOA radiances as the "measurements", with fixed aerosol properties, and tested whether it can be distinguished within instrument uncertainty, from a series of comparison model radiances, using the four χ^2 test variables described in the previous section. Here is a brief summary of the results obtained so far for MISR observations at middle to high latitudes:

1) For non-absorbing particles, the aerosol optical depth can be retrieved over calm ocean to 0.05 or 10%, whichever is larger, even if the particle properties are poorly known. As particle absorption increases, sensitivity to optical depth degrades, and becomes dependent on particle size and optical depth. When the optical depth is less than 0.5 or if the particle characteristic radius is less than

about 0.8 μm, MISR optical depth sensitivity is better than 15% when the imaginary index of refraction is within the values expected for all common particle types except soot (see Table 1). Based on climatology, most ocean cases fall well within these favored limits.

2) According to the simulations, MISR should be able to distinguish three to four groups of effective radius across the natural range ("small", "medium", and "large"). Most of this sensitivity occurs for particles between 0.1 and about 1 μm in characteristic radius. This covers the range of particle sizes where the scattering phase functions change from fairly isotropic behavior to curves with well-developed forward and backward scattering peaks. The sensitivity to effective radius increases for higher optical depth, since there is more aerosol signal in these cases, and is greatest for less absorbing particles.

3) MISR sensitivity to index of refraction increases strongly with increasing optical depth. We can distinguish about two or three groups of real index of refraction values between 1.33 and 1.55, as long as the optical depth is 0.1 or larger and the particles are not strongly absorbing. However the data are insensitive to the real part of the index of refraction for dark particles (imaginary index larger than about 0.01). Sensitivity to the imaginary part of the index of refraction follows a similar pattern, though the simulations suggest that three to four groups of values between 0.0 and 0.5 can be distinguished.

4) Because MISR can sample the aerosol phase function between scattering angles of 60° and 170°, the instrument is expected to be very sensitive to particle shape. For common mineral dust type aerosols, we can distinguish spherical from non-spherical particles over calm ocean with a range of sizes and column amounts expected under natural conditions.

More information about the sensitivity of MISR to aerosol properties over ocean can be found in [28] and [29].

V. AEROSOL RETRIEVAL OVER DENSE DARK VEGETATION

Techniques for retrieving aerosol column amount over land from space are considerably less well developed than those over dark water because of the higher brightness and heterogeneity of the land surface. The simplest means of determining the atmospheric contribution to the satellite signal is to make an assumption about the surface reflectivity or albedo. Locations where the sur-

face boundary condition is believed to be reasonably well understood are areas covered by dense, dark vegetation (DDV). A method based on imaging over DDV has been investigated [30] and forms [he basis of the MODIS aerosol retrieval over land [31]. MISR adopted a modified form of this approach whereby the low reflectance of dense vegetation in the 446 and 672 nm bands are constrained by a surface model, similar to the method used for retrievals over dark water. For DDV, however, only the angular reflectance shape of the surface model is specified, and the absolute reflectance in the blue and red bands are allowed to vary as free parameters (within certain limits). Therefore, as is the case for dark water, MISR's multi-view-angle capability can provide enhancements to single-view-angle approaches to aerosol retrievals over DDV.

A. Detection of DDV.

Before the "DDV" aerosol retrieval technique can be used, specific subregions must first be identified as DDV. This identification can be accomplished by comparing a subregion's computed ground-level vegetation index to a threshold value. The standard Normalized Difference Vegetation Index (NDVI) can be defined for MISR spectral bands as

$$\mathrm{NDVI} = \frac{'866 - '672}{L_{866} + L_{672}} \qquad \textbf{(lo)}$$

where L_{866} is the near-infrared surface-leaving radiance at 866 nm and L_{672} is the corresponding red radiance at 672 nm. In general the two wavelengths straddle the photosynthetic absorption edge so that L_{672} is significantly smaller than L_{866} for DDV. Therefore, if the two radiances are measured at ground level, the NDVI is close to unity for dense, dark vegetation. Here, DDV is defined such that any direct ground reflectance is completely obscured by the vegetation and that the strong photosynthetic absorption at the red wavelength guarantees a very low reflectance compared to the near-infrared.

If the radiance measurements L_{866} and L_{672} are made from a spacecraft instead of at ground level, then the inevitable atmospheric contamination of both radiances will modify the value of the NDV1 when compared to the ground level value. The atmosphere-contaminated NDVI for a given DDV site is generally smaller than the corresponding ground level NDVI, due mainly to the atmospheric path radiance contribution to the measured radiance at the red wavelength. In general, the NDVI will decrease as view zenith angle increases for DDV, due to the increased atmospheric con-

tribution. This characteristic forms the basis for a DDV detection algorithm which can be described as follows: when atmospherically contaminated NDVI values are plotted as a function of $1/\mu$, and the curve is extrapolated to the hypothetical viewing geometry $1/\mu = O$, the extrapolated NDVI value is theoretically the same as the extrapolated value obtained in the absence of atmospheric contamination [32]. This is due to the fact that L_λ^{atm} and T_λ both tend to zero when $1/\mu$ tends to zero, resulting in $L\acute{a}^{OA}$ being equal to L_λ^{surf} at $1/\mu = O$. The subregions which are classified as DDV are those for which the extrapolated NDVI is >0.75. Examples of the use of this algorithm are shown in Table 3.

B. Surface Contribution to TOA Reflectance

The surface contribution to the TOA radiance, $^{s}L_\lambda^{surf}$, in the dark water retrieval algorithm is easily computed using the aerosol components $L_{\lambda,n}^{surf}$ in the SMART dataset. In the DDV retrieval algorithm, however, L_λ^{surf} *is* explicitly computed from (2) in the blue (446 nm) and red (672 nm) MISR bands, using a parametrized surface reflectance model and atmospheric parameters in the SMART dataset. This method for computing L_λ^{surf} is quite general and not restricted to a particular surface model.

The model we used to describe the DDV surface bidirectional reflectance is that of Rahman et al. [33]:

$$R_\lambda^{surf}(-\mu, 1+),@\ ^{-}\phi_0)^{=} r_{0,\lambda}[\mu_0\mu(\mu+\mu_0)]^{k-1} \text{“} \frac{(1-\$^2)}{[1+g^2-2g\cos\Omega]^{3/2}} \cdot \left[1+\frac{1-r_{0,hot}}{1+G}\right] \quad (11)$$

where Ω is the scattering angle, defined by

$$\cos\Omega = -\mu\mu_0 + (1-\mu^2)^{\frac{1}{2}}(1-\mu_0^2)^{\frac{1}{2}}\cos(\phi-\phi_0), \quad (12)$$

and the geometric factor G is given by

$$G = \left\{\left(\frac{1}{\mu^2}-1\right)+\left(\frac{1}{\mu_0^2}-1\right)+2\left[\sqrt{\left(\frac{1}{\mu^2}-1\right)\left(\frac{1}{\mu_0^2}-1\right)}\right]\cos(\phi-\phi_0)\right\}^{\frac{1}{2}} \quad (13)$$

The adjustable parameters in (11) are $r_{0,\lambda}$, k, g, and $r_{0,hot}$. The last factor on the right hand side of (11) is included to model the "hot spot" for vegetation canopies, i.e., the brightness increase which occurs near scattering angles of 180° (backscatter). The parameter $r_{0,hot}$ in this factor is set to a fixed value of 0.015 which is typical for DDV. The variables k and g are also pre-specified and assumed to be wavelength independent, whereas $r_{0\lambda}$ is permitted to vary within narrow limits for both the blue and red MISR bands. Based on fits of (11) to measured [34] - [38] and synthetic [39], [40] DDV reflectance factor data sets [41], recommend values for k and g are 0.5 and -0.2, respectively, with an associated variance for each of about 0.02. Thus, it is convenient to rewrite (11) as

$$R_{\lambda}^{surf}(-\mu, \mu_0, \phi - \phi_0) = r_{0,\lambda}\hat{R}^{surf}(-\mu, \mu_0, \phi - \phi_0) \tag{14}$$

where $\hat{R}^{surf}$ represents a prescribed, wavelength independent, normalized BRF that defines the angular properties of the surface reflectance.

To make the calculations in *(2)* efficient, the surface BRF and the upward and downward diffuse transmittance are expanded as a cosine Fourier series in $\phi - \phi_0$. It then is assumed that only the first two terms in these expansions contribute significantly to the angular structure of the diffusely transmitted radiation fields incident on the surface and exiting at the TOA. The full functional form of the BRF, however, is used for directly transmitted light. Thus, the radiance incident at the surface can be approximated by

$$\begin{aligned} L_{\lambda}^{inc}(\mu, \mu_0, \phi - \phi_0; \tau_\lambda) \cong\ & E_{0,\lambda} \cdot e^{-\tau_\lambda/\mu_0} \cdot \delta(\mu - \mu_0) \cdot \delta(\phi - \phi_0) \\ & + E_{0,\lambda} \cdot [\bar{T}_{\lambda,0}(\mu, \mu_0; \tau_\lambda) + \bar{T}_{\lambda,1}(\mu, \mu_0; \tau_\lambda)\cos(\phi - \phi_0)] \\ & + \frac{r_{0,\lambda}\alpha \cdot s_\lambda(\tau_\lambda)}{\pi} \cdot \frac{E_{\lambda}^{dir}(\mu_0; \tau_\lambda) + E_{\lambda}^{diff}(\mu_0; \tau_\lambda)}{1 - r_{0,\lambda}\alpha \cdot s_\lambda(\tau_\lambda)} \end{aligned} \tag{15}$$

where δ is the Dirac delta function, $E_{.\lambda}$ is the TOA solar irradiance, $\bar{T}_{\lambda,0}$ and $\bar{T}_{\lambda,1}$ are the first two Fourier coefficients of the downward diffuse transmittance TX, s_λ is the bottom-of-atmosphere bihemispherical albedo, and a is given by

$$a = 4\int_0^1\int_0^1 \hat{R}_0^{surf}(-\mu', \mu)\mu'\mu d\mu' d\mu \qquad \textbf{(16)}$$

Here, $\hat{R}_0^{surf}$ is the first Fourier coefficient of $\hat{R}^{surf}$, with the first two coefficients defined as

$$\hat{R}_0^{surf}(-\mu, \mathbf{p'}) = \frac{1}{2\pi}\int_0^{271} \hat{R}^{surf}(-\mu', \mu, \phi' - \phi)d\phi', \qquad (17)$$

and

$$\hat{R}_1^{surf}(-\mu, \mu') = \frac{1}{\pi}\int_0^{2\pi} \hat{R}^{surf}(-\mu', \mu, \phi' - \phi)\cos(\phi' - \phi)d\phi'. \qquad (18)$$

Equivalent expressions define the two coefficients of the downward transmittance $\overline{T_\lambda}$. Finally, E_λ^{dir} and E_λ^{diff} *are* the direct and diffuse irradiances, respectively, at the bottom of the atmosphere for a black surface, with

$$E_\lambda^{dir}(\mu_0;\tau_\lambda) = E_{0,\lambda}\mu_0 e^{-\tau_\lambda/\mu_0}$$
$$E_\lambda^{diff}(\mu_0;\tau_\lambda) = 2\pi E_{0,\lambda}\int_0^1 \bar{T}_{\lambda,0}(\mu, \mu_0;\tau_\lambda)\mu d\mu \qquad (19)$$

The first term on the right-hand-side of (15) represents the direct radiance, the second term represents approximately the diffuse downwelling radiance in the absence of any surface reflectance (i.e., a black surface), and the last term represents approximately the downwelling radiance due to multiple reflections between the atmosphere and the surface. Using this expression and (14) in (2) and noting that the upward diffuse transmittance T_λ *is* related to the downward diffuse transmittance via reciprocity, i.e.,

$$\mu' T_\lambda(-\mu', -\mu, \phi' - \phi;\tau_\lambda) = \mu \bar{T}_\lambda(\mu, \mu', \phi - \phi';\tau_\lambda), \qquad \textbf{(20)}$$

the surface contribution to the TOA radiance can be written as

$$L_\lambda^{surf}(-\mu, \mu_0, \phi - \phi_0;\tau_\lambda) = r_{0,\lambda}\hat{L}_\lambda^{surf}(-\mu, \mu_0, \phi - \phi_0;\tau_\lambda) \tag{21}$$

where

$$\begin{aligned}
\hat{L}_\lambda^{surf}(-\mu, \mu_0, \phi - \phi_0;\tau_\lambda) = {} & \frac{E_\lambda^{dir}(\mu_0;\tau_\lambda)}{\pi} e^{-\tau_\lambda/\mu}\hat{R}^{surf}(-\mu, \mu_0, \phi - \phi_0) \\
& + \frac{E_{0,\lambda}}{\pi}\mu_0 e^{-\tau_\lambda/\mu}[f_{\lambda,0}(-\mu, -\mu_0;\tau_\lambda) + f_{\lambda,1}(-\mu, -\mu_0;\tau_\lambda)\cos(\phi - \phi_0)] \\
& + \frac{E_{0,\lambda}}{\pi}\mu_0 e^{-\tau_\lambda/\mu_0}[g_{\lambda,0}(-\mu, -\mu_0;\tau_\lambda) + g_{\lambda,1}(-\mu, -\mu_0;\tau_\lambda)\cos(\phi - \phi_0)] \\
& + \frac{E_{0,\lambda}}{\pi}\mu_0[h_{\lambda,0}(-\mu, -\mu_0;\tau_\lambda) + h_{\lambda,1}(-\mu, -\mu_0;\tau_\lambda)\cos(\phi - \phi_0)] \\
& + \frac{r_{0,\lambda}\alpha \cdot s_\lambda(\tau_\lambda)}{1 - r_{0,\lambda}\alpha \cdot s_\lambda(\tau_\lambda)} \frac{[E_\lambda^{dir}(\mu_0;\tau_\lambda) + E_\lambda^{diff}(\mu_0;\tau_\lambda)]}{\pi} \cdot [e^{-\tau_\lambda/\mu}A(-\mu) + a_{\lambda,0}(-\mu;\tau_\lambda)]
\end{aligned} \tag{22}$$

and

$$f_{\lambda,0}(-\mu, -\mu_0;\tau_\lambda) = 2\pi\int_0^1 \hat{R}_0^{surf}(-\mu, \mu')T_{\lambda,0}(-\mu_0, -\mu';\tau_\lambda)d\mu', \tag{23}$$

$$f_{\lambda,1}(-\mu, -\mu_0;\tau_\lambda) = \pi\int_0^1 \hat{R}_1^{surf}(-\mu, \mu')T_{\lambda,1}(-\mu_0, -\mu';\tau_\lambda)d\mu', \tag{24}$$

$$g_{\lambda,0}(-\mu, -\mu_0;\tau_\lambda) = 2\pi\int_0^1 T_{\lambda,0}(-\mu, -\mu';\tau_\lambda)\hat{R}_0^{surf}(-\mu_0, \mu')d\mu', \tag{25}$$

$$g_{\lambda,1}(-\mu, -\mu_0;\tau_\lambda) = \pi\int_0^1 T_{\lambda,1}(-\mu, -\mu';\tau_\lambda)\hat{R}_1^{surf}(-\mu_0, \mu')d\mu', \tag{26}$$

$$h_{\lambda,0}(-\mu, -\mu_0;\tau_\lambda) = 2\pi\int_0^1 T_{\lambda,0}(-\mu, -\mu';\tau_\lambda)f_{\lambda,0}(-\mu', -\mu_0;\tau_\lambda)d\mu', \tag{27}$$

$$h_{\lambda,1}(-\mu, -\mu_0;\tau_\lambda) = \pi\int_0^1 T_{\lambda,1}(-\mu, -\mu';\tau_\lambda)f_{\lambda,1}(-\mu', -\mu_0;\tau_\lambda)d\mu', \tag{28}$$

$$a_{\lambda,0}(-\mu;\tau_\lambda) = 2\pi\int_0^1 T_{\lambda,0}(-\mu,-\mu';\tau_\lambda)A(-\mu')d\mu', \quad (29)$$

and

$$A(-\mu) = 2\int_0^1 \hat{R}_0^{surf}(-\mu,\mu')\mu' d\mu'. \quad (30)$$

Combining (21) and (22) we note that all terms describing L_λ^{surf} are linear in $r_{0,\lambda}$ except for the last one. Linearity, however, is desirable in order to make the retrievals computationally efficient. Fortunately, since the product of $r_{0,\lambda}$ and s_λ is small for DDV, the last term in (22) can be reasonably approximated by specifying a fixed value for $r_{0,\lambda}$ equal to 0.01 5.

The functions *a, A,* $\hat{R}_0^{surf}$, $\hat{R}_1^{surf}$, and those expressed by (23) - (29) are computed as needed during the retrieval process. However, the two functions, $T_{\lambda,0}$ and $T_{\lambda,1}$, used in these expressions are precomputed and stored in the SMART dataset for each pure aerosol type, evaluated on a standard grid of aerosol optical depths and on a standard Radau quadrature point grid for μ and μ', which greatly simplifies the mathematical integration operation in these. equations. E_λ^{cliff} and s_λ, parameters also needed by the algorithm, are evaluated on the same optical depth and quadrature point grids, and included in the SMART dataset.

Like the aerosol retrieval over ocean, standard linear mixing is used to compute the surface contribution to the TOA radiance. The contributions for the individual components of the aerosol mixture are computed using (22).

C. Criteria for Aerosol Best Estimate

Similar criteria as for "dark water" retrieval case are used here. Median radiances are determined using all DDV subregions within the region, and these radiances then are compared to the selected model aerosol mixture/surface TOA radiances. However, there are several notable differences:

(1) The sum over wavelength includes only the blue (446 nm) and red (672 nm) MISR bands at which DDV has the lowest reflectance;

(2) The aerosol column amount and the BRF parameters $r_{0,\lambda}$ in the blue and red bands arc varied in order to minimize the χ^2_{abs} parameter. The other χ^2 metrics are then calculated for these optimal values of optical depth and surface reflectances;

(3) The σ^2_{abs}, σ^2_{geom}, and σ^2_{spec} are modified to include uncertainty in the assumed shape of the surface BRF:

(4) The χ^2_{maxdev} testis not used;

(5) For χ^2_{abs}, χ^2_{geom}, and χ^2_{spec}, the threshold value for an acceptable fit is taken to be 3.

The latter four differences reflect the greater uncertainty in specification of the surface boundary condition relative to the dark water retrieval case.

The criterion used to determine the best fitting aerosol model is the minimization of χ^2_{abs}, in (3), where L^{TOA}_{λ} is now given by

$$L^{TOA}_{\lambda}(-\mu, \mu_0, \phi - \phi_0;\tau_{\lambda}) = L^{atm}_{\lambda}(-\mu, \mu_0, \phi - \phi_0;\tau_{\lambda}) + r_{0,\lambda}\hat{L}^{surf}_{\lambda}(-\mu, \mu_0, \phi - \phi_0;\tau_{\lambda}). \qquad (31)$$

The parameter $r\text{-}o,_{\lambda}$ is adjusted in this definition of χ^2_{abs}, such that χ^2_{abs} is minimized for each point on the τ_{558} grid. This is done by a least squares procedure, whereby

$$r_{0,\lambda} = \frac{\sum_j \frac{w_{\lambda j} \cdot [L^{MISR}_{\lambda}(j) - L^{atm}_{\lambda}(j;\tau_{\lambda})]\hat{\rho}^{surf}_{\lambda}(j;\tau_{\lambda})}{\sigma^2_{abs,\lambda}(j)}}{\sum_j \frac{w_{\lambda j} \cdot [\hat{L}^{surf}_{\lambda}(j;\tau_{\lambda})]^2}{\sigma^2_{abs,\lambda}(j)}}, \qquad (32)$$

with the requirement that $r_{0\lambda}$ falls within specified limits, namely $0 \leq r_{0,\lambda} < 0.03$. If $r_{0,\lambda}$ as determined from (32) is less than O, it is replaced by O, and if it is greater than 0.03, it is replaced by 0.03. In calculating χ^2_{abs} and $r_{0\lambda}$, σ^2_{abs} is modified to include the uncertainty in $\hat{L}^{surf}_{\lambda}$ due to the uncertainties in the surface model parameters *k* and *g*. Assuming no correlation between the measurement and model uncertainties, the modified σ^2_{abs} can be approximated by

$$\sigma^2_{abs,\lambda}(j) \Rightarrow \sigma^2_{abs,\lambda}(j) + [q_k^2(j) + q_g^2(j)][r_{0,\lambda}\hat{L}_\lambda^{surf}(j;\tau_\lambda)]^2 \tag{33}$$

where

$$q_k^2(j) = \sigma_k^2 \cdot \ln^2[\mu_0\mu_j(\mu_j + \mu_0)]$$

$$q_g^2(j) = \sigma_g^2 \cdot \left[\frac{2g}{1-g^2} + \frac{3[g - \cos\Omega_j]}{1 + g^2 - 2g\cos\Omega_j}\right]^2 \tag{34}$$

The functions q_k^2 and q_g^2 were derived for the surface model of (11); σ_k^2 and σ_g^2 are the variances associated with the values for *k* and g, respectively. Note that σ^2_{abs} in (32) now also depends on r_0 via (33). This dependence, however, was ignored in the derivation of (32) since it has minimal impact on the derived best-fitting values of $r_{0\lambda}$. Therefore, a set value of 0.015 for $r_{0,\lambda}$ is used in the expression for σ^2_{abs}.

Once χ^2_{abs} is determined as a function of τ_{558}, the minimum value of χ^2_{abs} and its corresponding optical depth, $\tau_{558}^{bestfit}$ and uncertainty $\Delta\tau_{558}^{bestfit}$, are then found, using the parabolic curve fitting procedure described previously. This aerosol optical depth, along with the values of $r_{0,\lambda}$ associated with the minimum χ^2_{abs}, are then used with (3 1) to compute the other two metrics, χ^2_{geom} and χ^2_{spec}. An aerosol model is determined to be a good fit to the data when all three metrics have values ≤ 3.

D. Aerosol Retrieval Simulations

To test how well the algorithm is expected to perform, a sensitivity study was done using simulated MISR datasets in which the atmospheric aerosol varied with both column amount and type. The DDV detection scheme, described in Section *A*, was also used as part of the retrieval simulation.

The aerosol type used to simulate the MISR measurements was a sulfate/nitrate composition at RH 70% with an effective radius, r_{eff}, of 0.21 μm, similar to the Sulfate/nitrate l model in the APOP file of the Aerosol Climatology Product (see Table l) but with smaller particles. Three aerosol column amounts were considered, characterized by optical depths of 0.1, 0.25, and 0.5 at 558 nm. Simulated data were produced for three solar zenith angles, 25°,45°, and 65°, with the azimuth

angles of the MISR views set at values which are typical for those zenith angles. Eleven different surface types were used with directional reflectance properties based on field measurements [35] - [37]. The multiple scattering calculations were performed using a matrix operator technique [42], where Rayleigh scattering was included along with the aerosol scattering and the bidirectional reflectance of the various surface types and all orders of surface-atmosphere reflections were taken into account. The simulated MISR radiances also include the noise properties expected from the MISR instrument [27], characterized by the parameters σ^2_{abs}, σ^2_{geom}, and σ^2_{spec}. In Table 3 the surface types are listed along with (1) their NDVI in the nadir view, (2) the extrapolated NDVI for the case where the atmosphere is absent, and (3) the extrapolated NDVI for the three aerosol column amounts. The chosen sun angle is 45°. Note that for those cases which are classified as DDV (cases 5,6,7,8, and 10 for which the extrapolatedNDVI20.75), the extrapolated NDVI (no atmosphere) is generally larger than the nadir view NDVI (no atmosphere), due to a consistently decreasing NDV1 with increasing view angle. For the DDV cases the extrapolated NDVI (variable aerosol optical depth) is also quite consistent with the extrapolated NDVI (no atmosphere), illustrating the use of the extrapolated NDVI as an accurate indicator of DDV targets when aerosol is present. The median value of the identified DDV target radiances for each camera view and for the 446 and 672 nm MISR bands was used as the input to the aerosol retrieval algorithm.

In the aerosol retrieval sensitivity study, the candidate aerosols included the correct RH 70% sulfate/nitrate model (r_{eff} = 0.21 μm), this sulfate/nitrate model at 90% RH (r_{eff} = 0.32 μm), and a selection of six other aerosol possibilities, taken from the APOP file. These additional models included: RH O% Sulfate/nitrate 2 (r_{eff} = 0.53 μm), RH 70% and 90% Sea Salt (accumulation mode; r_{eff} = 0.70 and 1.30 Pm, respectively), RI-I 70% Sea Salt (coarse mode; r_{eff} = 10.23 μm), and absorbing Mineral Dust (small and large particles; r_{eff} = 0.53 and 4.26 μm, respectively). These candidate models represent aerosol types with particle sizes and single scattering albedos different from the correct model and, therefore, will test the sensitivity of the algorithm to these aerosol properties. The retrieval results are shown in Tables 4, 5, and 6 for the solar zenith angles of 25°, 45°, and 65°, respectively. Those retrieved optical depths with an uncertainty of 0.00 in the tables are cases in which the minimum χ^2_{abs} occurred at a limiting value of the aerosol optical depth, i.e., either no aerosol or its maximum amount. This maximum amount requires a zero surface reflectance to satisfy the observations: any more would demand a negative surface reflectance in a least one of the multi-angle, multispectral observations since the aerosols are brighter than the surface in all cases. From the criteria that χ^2_{abs}, χ^2_{geom}, and χ^2_{spec} must each be ≤ 3 as an acceptable

fit (o [he observations, the first point to note is that good retrievals are obtained for all aerosol column amounts and solar zenith angles when the correct candidate model (RH 70% Sulfate/nitrate1) is used. Secondly, these tables clearly show that sensitivity to the aerosol model type increases with increasing column amount and increasing solar zenith angle. For example, in Table 4 (solar zenith angle θ_0 = 25°) for an optical depth of 0.1, five of [he eight candidate models have acceptable fits, whereas only two models fit well for the optical depths 0.25 and 0.50. These results also show that the non-correct but successful candidate models produce optical depths which can be substantially different than the correct one. When θ_0 increases to 45° (Table 5) only two of the candidate models (the correct model and its 90% RH counterpart) produce acceptable fits for optical depths 0.1 and 0.25 and only the correct aerosol model is acceptable for optical depth 0.50. Also note that the retrieved optical depths for the two successful models agree more closely than for these same two models when θ_0 is 25°. Finally, in Table 6 (θ_0 = 65°) only the correct aerosol type is a successful model for all three optical depths.

VI. AEROSOL, RETRIEVAL OVER HETEROGENEOUS LAND

Since dense, dark vegetation is found only over a portion of the land surface, other methods are required to extend the aerosol retrieval spatial coverage. Separability of the surface-leaving and atmosphere-leaving signals over terrain with heterogeneous surface reflectance is the objective of several methods developed by the MISR team [43] - [46]. The “heterogeneous land” algorithm differs from the “dark water” and “DDV” algorithms in that it does not rely on the presence of a particular, well described surface type, but instead uses the presence of spatial contrasts within the 17.6 km retrieval region to derive an empirical orthogonal function (EOF) representation of the region-averaged surface contribution to the TOA radiances. This is the most general of the three techniques and it uses all four MISR spectral bands in the analysis.

A. Surface Contribution to TOA Reflectance

For the retrieval of aerosol over heterogeneous land [46], we use the surface contribution $\langle L_\lambda^{surf} \rangle$, averaged over the individual subregions of a 17.6 km region. This average can be expressed as

$$\langle L_\lambda^{surf}(-\mu, \mu_0, \phi - \phi_0)\rangle = \sum_{n=1}^{N_\lambda} A_{n,\lambda} \cdot f_{n,\lambda}(-\mu, \mu_0, \phi - \phi_0), \tag{35}$$

where $f_{n\lambda}$ *are* empirical orthogonal functions, derived from the individual subregion radiances. These EOF'S are the eigenvectors of a scatter matrix C_λ, with elements

$$C_{\lambda\, ij} = \sum_{x,\, y} [L_{\lambda,\, x,\, y}^{MISR}(i) - \langle L_\lambda^{MISR}(i)\rangle][L_{\lambda,\, x,\, y}^{MISR}(j) - \langle L_\lambda^{MISR}(j)\rangle] \quad i,\ j = 1, \ldots,\ N_{cam} \tag{36}$$

where the x, y summation is over all the cloud-free subregions within the region, $\langle L_\lambda^{MISR}\rangle$ is the average MISR radiance of the region for a camera with an angular view designated by i or j, and N_{cam} is the number of camera views used. Since the atmospheric path radiance L_λ^{atm} is assumed constant over the region, it can be seen from (1) that the process of subtracting $\langle L_\lambda^{MISR}\rangle$ from the individual subregion radiances $L_{\lambda,\, x,\, y}^{MISR}$ results in C_λ being a function only of L_λ^{surf}, which generally varies with location, x, y.

There are N_λ free parameters $A_{n,\lambda}$ in (35) that are adjusted during the process of comparing measurements to model radiances. Since the eigenvectors form a complete basis vector set, the number of eigenvectors, N_λ, used in the summation must be less than the total number of eigenvectors (i.e., number of cameras used, N_{cam}).

B. Criteria for Aerosol Best Estimate

The criterion used to determine the best fitting aerosol model is the minimization of the test variable χ_N^2, defined as

$$\chi_N^2(\tau_{558}) = \frac{\sum_\lambda \sum_j \nu_\lambda(j) \cdot \dfrac{\left(\langle L_\lambda^{MISR}(j)\rangle - L_\lambda^{atm}(j;\tau_\lambda) - \sum_{n=1}^{N_\lambda} A_{n,\lambda} \cdot f_{n,\lambda}(j)\right)^2}{\sigma_{hetero,\lambda}^2(j)}}{\sum_\lambda \sum_j \nu_\lambda(j)}, \tag{37}$$

where the summation is over the nine MISR view angles and four wavelengths, L_λ^{atm} is the path radiance of the model aerosol mixture, and $\sigma_{hetero,\lambda}^2$ is the estimated variance of the N_λ term

summation. The weight $\nu_\lambda = 1$ if a valid values of $\langle L_\lambda^{MISR} \rangle$ exists, otherwise $\nu_\lambda = O$. For each τ_{558} on the optical depth grid, the expansion coefficients $A_{n\lambda}$ are varied to minimize the summation factor in a least squares sense. Their values are easily obtained by applying the orthonormality condition of the eigenvectors to the bracketed expression in (37), i.e.,

$$A_{n,\lambda} = \sum_j [\langle L_\lambda^{MISR}(j) \rangle - L_\lambda^{atm}(j;\tau_\lambda)] \text{ “ } f\text{“, ~(j).} \tag{38}$$

The contribution of an individual eigenvector in describing the angular shape of $\langle L_\lambda^{surf} \rangle$ is determined by the relative size of its eigenvalue. The eigenvectors are ordered such that the corresponding eigenvalues $e_{n\lambda}$ decrease monotonically, i.e., $e_{1\lambda} > e_{2\lambda} > \ldots > e_{N_{cam},\lambda}$. Therefore, only those eigenvectors with eigenvalues greater than or equal to a certain size are used in the summation in (35). The maximum number of usable eigenvectors N_{max} is determined by the condition

$$e_{N_{max},\lambda} \leq 2e_{N_{cam},\lambda} < e_{N_{max}-1,\lambda} \tag{39}$$

where $2e_{N_{cam},\lambda}$ is twice the smallest eigenvalue and approximates the noise threshold of the image. Eigenvalues smaller than this threshold have eigenvectors which contribute essentially noise to the angular variability of the region. Given N_{max}, the variance $\sigma^2_{remain\,\lambda}$ associated with the unused eigenvalues is given by

$$\sigma^2_{remain,\lambda} = \frac{1}{N_{cam}N_{sub}} \cdot \sum_{n=N_{max}+1}^{N_{cam}} e_{n,\lambda} \tag{40}$$

where N_{sub} is the number of subregions used to generate the eigenvectors. Therefore, $\sigma^2_{hetero,\lambda}$ in (37) can be written as

$$\sigma^2_{hetero,\lambda}(j) = \sigma^2_{remain,\lambda} \cdot \left[\frac{\langle L_\lambda^{MISR}(ref) \rangle - L_\lambda^{atm}(ref;\tau_\lambda)}{\langle L_\lambda^{MISR}(ref) \rangle - L_\lambda^{atm}(ref;\tau_\lambda^{Ray})} \right]^2 . \tag{41}$$

Since $\langle L_\lambda^{MISR} \rangle - L_\lambda^{atm}$ continuously decreases with increasing model aerosol optical depth, the associated variance $\sigma^2_{hetero\,\lambda}$ also is correspondingly reduced, referenced to the case of no aerosol (i.e, only Rayleigh scattering, $\tau_\lambda = \tau_\lambda^{Ray}$) and to a particular reference camera, *ref,* normally nadir.

For each of the candidate aerosol models a χ^2_N is computed for each value of N used in (37), starting with $N = 1$ (use of [he first eigenvector only) and incrementing the number of eigenvectors in each wavelength band simultaneously by unity but not letting the number in any given wavelength band exceed N_{max}. The minimum χ^2_N for each value of N, $\chi^2_{N,min}$, and the associated parameters $\tau_{N\,558}$, and $\Delta\tau_{N\,558}$, expressed by Eqs. (5) and (6), respectively, are then found using the parabolic curve fitting procedure.

For the aerosol model being evaluated, the reported best-fitting optical depth is computed from a weighted average of all N_{max} optical depths, $\tau_{N\,558}$,

$$\tau_{558}^{bestfit} = \frac{\sum_{N=1}^{N_{max}} \frac{\tau_{N,558}}{\chi^2_{N,min}}}{\sum_{N=1}^{N_{max}} \frac{1}{\chi^2_{N,min}}} \tag{42}$$

where the weights are the inverses of the $\chi^2_{N,min}$. The formal uncertainty associated with $\tau_{558}^{bestfit}$ is then expressed as

$$\Delta\tau_{558}^{bestfit} = \frac{\sqrt{\sum_{N=1}^{N_{max}} \frac{\Delta\tau_{N,558}}{\chi^2_{N,min}}}}{\sum_{N=1}^{N_{max}} \frac{1}{\chi^2_{N,min}}} \tag{43}$$

Finally, the effective χ^2_{hetero} associated with $\tau_{558}^{bestfit}$ is defined as the weighted average of all of the $\chi^2_{N,min}$,

$$\chi^2_{hetero}(\tau_{558}^{bestfit}) = \frac{N_{max}}{\sum_{N=1}^{N} \frac{1}{\chi^2_{N,min}}} \tag{44}$$

We consider successful aerosol models to be those for which $\chi^2_{hetero} \leq 3$.

C. Aerosol Retrieval Simulations

A sensitivity study, similar to that for the "DDV" algorithm, was performed for the same atmospheric conditions, surface BRF types, and sun geometries. However, a scene of the Wind River Basin in Wyoming from Landsat imagery was used to pattern the surface pixel albedo variability in the simulated MISR multiangle imagery. Two limiting cases relating pixel brightness (i.e., albedo) to BRF type were considered. One case (random) had randomly assigned BRF types (from the list of eleven types in Table 3) to the pixels in the scene. The other case (correlated) assigned a particular BRF type to a pixel, depending on the pixel brightness. It is expected that a real scene would exhibit albedo-BRF characteristics which fall somewhere between these limiting cases. Each simulated MISR image was 256x256 pixels in size, which was subsequently subdivided into 16x 16 subimages, each 16x 16 pixels in size. Each of these 256 multi-angle subimages was then analyzed using the "heterogeneous land" retrieval algorithm. For the random surface property case, an aerosol optical depth of 0.5 and a sun angle of 45°, the set of eigenvalues for a typical subimage are listed in Table 7. The criterion for selecting the number of eigenvectors to be use in the analysis of a given subimage is described by (39). For the eigenvalues in Table 7, the maximum number of selected eigenvectors is five and for the other associated 255 subimages, the maximum number ranged from three to six.

The results of the retrievals are shown in Tables 8,9, and 10 for solar zenith angles of 25°, 45°, and 65°, respectively. The results of the random BRF -albedo selection case were very similar to the correlated case and so only the correlated case is shown here. Also, since 256 subimages were separately analyzed within the image with the algorithm, the retrieved optical depths $\tau^{bestfit}$ and the best fit parameters χ^2_{hetero} listed in the tables represent averages of these subimages. Applying the criterion that χ^2_{hetero} be less than or equal to 3 as an acceptable fit to the observations, the results are similar to those for the DDV algorithm, indicating equivalent sensitivities to both aerosol column amount and type.

VII. DISCUSSION AND CONCLUDING REMARKS

The three aerosol retrieval algorithms described in this paper will be available at time of launch to begin the arduous task of processing the MISR data taken over the globe on a routine basis. These algorithms have some attributes in common and others which are unique to the par-

ticular type of observed surface conditions. For observations taken over ocean or dark water, the "dark water" retrieval algorithm is used and is considered to be the most accurate of the three algorithms. Here the surface condition is assumed to be completely known, i.e., (here are no free parameters. and therefore should contribute minimal uncertainty to the aerosol retrieval results. This algorithm will undoubtedly be the most used in a global sense but the least used when over land, since dark lakes on the order of 5 kilometers or more in size (a pre-requisite for using the algorithm) are not common. In the absence of land-based dark water bodies, the "DDV" retrieval algorithm will be used when dense, dark vegetation is identified, and is probably the next most accurate algorithm. There is one free parameter per spectral band in its description of the surface condition, the reflectivity parameter $r_{0\lambda}$. Therefore, when compared to the "dark water" algorithm, it should not be quite as sensitive to the atmospheric condition. Finally, the "heterogeneous land" algorithm is used when the other two algorithms have been excluded, and of the three algorithms its overall accuracy is the least well characterized at present. The surface condition for this algorithm is described by an empirical orthogonal function series with about four or five terms. Since the number of free parameters per spectral band equals the number of terms used, this algorithm has considerable flexibility in describing the surface contribution to the TOA radiance and in principle, it has less sensitivity than the other two algorithms to the atmospheric path radiance. It has the benefit, however, of using an angular description of the surface which is derived directly from the multi-angular data, whereas the other two algorithms rely on the accuracy of the predetermined angular characteristics of their surface models. This is probably the reason the "heterogeneous land" algorithm compared so well to the "DDV" algorithm in the aerosol retrieval tests.

A considerable amount of effort will be spent investigating the accuracy of these algorithms immediately after MISR data become available. Our results will be compared directly with those from other EOS instruments, e.g., MODIS, other satellite instruments, and to the aerosol climatologies. Selected areas over the globe will be identified in which all three algorithms can be used, thus allowing a detailed intercomparison of retrieval results. Other sites have extensive aerosol monitoring equipment, e.g., [47] which allows a comparison of their retrieval results with those from a simultaneous MISR overpass. There will also be an ongoing series of MISR-specific validation campaigns around the Southern California area and large, but less frequent, EOS validation campaigns at selected sites and involving various EOS instrument groups. All these opportunities will be used to test and improve the MISR retrieval algorithms, eventually resulting in global, monthly maps of aerosol distribution along with daily regional coverage.

ACKNOWLEDGMENT

This research was carried out by the Jet Propulsion Laboratory, California Institute of Technology, under contract with the National Aeronautics and Space Administration.

REFERENCES

[1] R.J. Charlson, S.E. Schwartz, J.M. Hales, R.D. Cess, J.A. Coakley Jr., J.E. Hansen and D.J. Hoffman, "Climate forcing by anthropogenic aerosols," Science. vol.255, pp. 423-430, 1992.

[2] J.T. Kiehl, and B.P. Briegleb, "The relative role of sulfate aerosols and greenhouse gases in climate forcing," *Science,* vol.260, pp. 311-314, 1993.

[3] M.O. Andrea, "Climate effects of changing atmospheric aerosol levels," In: *Future Climate of the World: A modelling perspective,* World Survey and Climatology, vol. XVI., A. Henderson-Sellers (cd.)., Elsevier, Amsterdam, 1995.

[4] IPCC WGII, *Climate Change 1995- Impacts, Adaptations and Mitigations of Climate Change: Scientific-Technical Analyses: The Second Assessment Report of the Inter-Governmental Panel on* Climate *Change,* R.T. Watson, M.C. Zinyowera, and R.H. Moss (eds.), Cambridge University Press, New, York, 1995.

[5] L.L. Stowe, A.M. Ignatov, and R.R. Singh, "Development, validation and potential enhancements to the second-generation operational aerosol product at the National Environmental Satellite, Data, and Information Service of the National Oceanic and Atmospheric Administration," *J. Geophys. Res.,* vol. 102, pp. 16,923-16,934, 1997.

[6] D.J. Diner, J. C. Beckert, T.H. Reilly, C.J. Bruegge, J.E. Conel, R.A. Kahn, J.V. Martonchik, T.P. Ackerman, R. Davies, S.A.W. Gerstl, H.R. Gordon, J.-P. Muller, R. Myneni, P. Sellers, B. Pinty, and M.M. Verstraete, "Multi-angle Imaging SpectroRadiometer instrument description and experiment overview," *IEEE Trans. Geosci. and Remote Sensing,* (this issue), 1998.

[7] G.A. d'Almeida, P. Koepke, and E. P. Shettle,. *Atmospheric Aerosols: Global climatology and radiative characteristics.* Deepak Publishing, 1991

[8] G.M. Krekov, "Models of atmospheric aerosols," in *Aerosol Effects on Climate, S. G.* Jennings, cd., University of Arizona Press, 1993.

[9] E.P. Shettle and R.W. Fenn, *Models for the aerosols of the lower atmosphere and the effects of humidity variations on their optical properties.* AFGL-TR-79-02*14,* Air Force Geophysics Laboratory, 1979.

[10] World Climate Programme WCP-112. *A Preliminary Cloudless Standard Atmosphere for Radiation Computation.* IAMAP (International Association for Meteorology and Atmospheric Physics), Boulder, CO, 1984.

[11] D.J. Diner, W.A. Abdou, H.R. Gordon, R.A. Kahn, Y. Knjazikhin, J.V. Martonchik, S.

McMuldroch, R. Myneni, R.A. West, *Level 2 Ancillary Products and Datasets Algorithm Theoretical* Basis. JPL D-13402, Rev. A., 1997.

[12] M.I. Mishchenko, A.A. Lacis, B.E. Carlson, and L.D. Travis, "Nonsphericity of dust-like tropospheric aerosols: Implications for aerosol remote sensing and climate modeling," *Geophys. Res. Lett.* vol. 22, pp. 1077-1080, 1995.

[13] M.I. Mishchenko, L.D. Travis, R.A. Kahn, and R.A. West, "Modeling phase functions for dust-like tropospheric aerosols using a shape mixture of randomly oriented polydisperse spheroids," *J. Geophys. Res., vol.* 102, pp. 16,831-16,848, 1997.

[14] M. Wang and H.R. Gordon, "Radiance reflected from the ocean atmosphere system: Synthesis from individual components of the aerosol size distribution," *Appl. Opt.,* vol. 33, pp. 7088-7095, 1994.

[15] W.A. Abdou, J.V. Martonchik, R.A. Kahn, R.A. West, and D.J. Diner, "A modified linear mixing method for calculating atmospheric path radiances of aerosol mixtures, " *J. Geophys. Res.,* vol. 102, pp. 16,883-16,888, 1997.

[16] R.S. Fraser, "Satellite measurement of mass of Sahara dust in the atmosphere," *Appl. Opt.,* vol. *15,* pp. *2471-2479, 1976.*

[17] M. Griggs, "Measurements of atmospheric aerosol optical thickness over water using ERTS-1 data," *J. Air Pollut. Control Assoc.,* vol. 25, pp. 622-626, 1975.

[18] M. Griggs, "Satellite measurements of tropospheric aerosols," *Adv. Space Res.,* vol. 2(5), pp. 109-118, 1983.

[19] C.S. Long and L. L. Stowe, "Using the NOAA/AVHRR to study stratospheric aerosol optical thickness following the Mt. Pinatubo eruption," *Geophys. Res. Lett.*, vol. 21, pp. 2215-2218, 1994.

[20] C.R.N. Rae, L. L. Stowe, and E. P. McClain, "Remote sensing of aerosols over the oceans using AVHRR data: Theory, practice and applications," *Int. J. Remote Sensing,* vol. 10, pp. 743-749, 1989

[21] L.L. Stowe, R. M. Carey, and P. P. Pellegrino, "Monitoring the Mt. Pinatubo aerosol layer with NOAA/1 1 AVHRR data," *Geophys. Res. Lett., vol.* 19, pp. 159-162, 1992

[22] M.I. Mishchenko and L.D. Travis, "Light scattering by polydisperse, rotationally symmetric nonspherical particles: Linear polarization, " *J. Quant. Spectrosc. Radiat. Transfer,* vol. *5* 1, pp. *759-778, 1994.*

[23] L. Tsang, J.A. Kong, and R.T. Shin, *Theory of Microwave Remote Sensing, Wiley, New* York, 1985.

[24] C. Cox and W. Munk, "Measurements of the roughness of the sea surface from photographs of the Sun's glitter," *J. Opt. Sot. Amer., vol. 44,* pp. 838-850,1954.

[25] P. Koepke, "Effective reflectance of oceanic whitecaps," *Appl. Opt., vol. 23,* pp. 1816-1824, 1984.

[26] E.C. Monahan and I.G. O'Muircheartaigh, "Optimal power-law description of oceanic whitecap coverage dependence on windspeed," *J. Phys. Oceanogr.,* vol. 10, pp. 2094-2099, 1980.

[27] C.J. Bruegge, N. L. Chrien, R.A. Kahn, J.V. Martonchik, and D.J. Diner, "Uncertainty tabulations for the retrieval of Aerosol and Surface Products," Conference issue: New Developments and Applications in Optical Radiometry (NEWRAD'97), *Metrologia* (in preparation).

[28] R. Kahn, R. West, D. McDonald, B. Rheingans, and M.I. Mishchenko, "Sensitivity of multiangle remote sensing observations to aerosol sphericity," *J. Geophys. Res.,* vol. 102, pp. 16,861-16,870, 1997.

[29] R. Kahn, P. Banerjee, and D. McDonald, "Sensitivity of multiangle imaging to aerosol optical depth, and to pure-particle size distribution and composition over ocean," *J. Geophys. Res.,* in preparation.

[30] Y.J. Kaufman and C. Sendra, "Algorithm for atmospheric corrections," *Int. J. Remote Sensing, vol. 9,* pp. 1357-1381, 1988.

[31] M.D. King, Y. J. Kaufman, W. P. Menzel, and D. Tanre, "Remote sensing of cloud, aerosol, and water vapor properties from the Moderate resolution Imaging Spectrometer (MODIS)," *IEEE Trans. Geosci. Remote Sensing,* vol. 30, pp. 2-27, 1992.

[32] J.V. Martonchik, "Atmospheric correction of vegetation index using multi-angle measurements," *Proceedings of the IGARSS '95 Symposium* (Firenze, Italy), 1995.

[33] H. Rahman, B. Pinty, and M.M. Verstraete, "Coupled Surface-Atmosphere Reflectance (CSAR) model. 2. Semiempirical surface model usable with NOAA Advanced Very High Resolution Radiometer data," *J. Geophys. Res., vol.* 98, pp. 20,791-20,801, 1993.

[34] D.W. Deering and P. Leone, "A sphere-scanning radiometer for rapid directional measurements of sky and ground radiance," *Remote Sensing Environment, vol. 19,* pp. 1-24, 1986.

[35] D.S. Kimes, "Dynamics of directional reflectance factor distributions for vegetation canopies," *Appl. Opt, vol.* 22, pp. 1364-1372, 1983.

[36] D.S. Kimes, W. Newcomb, C. Tucker, I. Zonneveld, W. van Wijngaarden, J. de Leeuw, and G. Epema, "Directional reflectance factor distributions for cover types of northern Africa in NOAA 7/8 AVHRR bands 1 and 2," *Remote Sensing Environment,* vol. 18, pp. 1-19, 1985.

[37] D.S. Kimes, W. W. Newcomb, R. F. Nelson, and J. B. Schutt, "Directional reflectance distributions of a hardwood and pine forest canopy," *IEEE Trans. Geosci. Remote Sensing,* vol. *GE-24,* pp. *281-293, 1986.*

[38] D.S. Kimes and W.W. Newcomb, "Directional scattering properties of a wintering deciduous hardwood canopy," *IEEE Trans. Geosci. Remote Sensing, vol. 25,* pp. 510-515, 1987.

[39] Y. Govaerts and M. M. Verstraete, "Applications of the L-systems to canopy reflectance modelling in a Monte Carlo Ray Tracing technique," in *Multispectral and Microwave Sensing of Forestry, Hydrology, and Natural Resources,* SPIE, Rome, 1994.

[40] R.B. Myneni and G. Asrar, "Radiative transfer in three-dimensional atmosphere-vegetation media," *J. Quant. Spectrosc. Radiat. Transfer, VO1.49,* pp. 585-598, 1993.

[41] O. Engelsen, B. D. Pinty, and M. M. Verstraete, "Parametric Bidirectional Reflectance Factor (BRF) models: I. Evaluation," Internal report, Institute for Remote Sensing Applications, Joint Research Centre, Ispra, Italy, 1996.

[42] I.P. Grant and G.E. Hunt, "Solution of radiative transfer problems using the invariant S_n method," *Mon. Not. Roy. Astron. Sot.,* vol. 141, pp. 27-41, 1968.

[43] D.J. Diner and J. V. Martonchik, "Atmospheric transmittance from spacecraft using multiple view angle imagery," *Appl. Opt.,* vol. 24, pp. 3503-3511, 1985.

[44] D.J. Diner, S.R. Paradise, and J.V. Martonchik, "Development of an aerosol opacity retrieval algorithm for use with multi-angle land surface images," *Proceedings of the IGARSS* '94 *Symposium* (Pasadena, CA), 1994.

[45] J.V. Martonchik and D. J. Diner, "Retrieval of aerosol optical properties from multiangle satellite imagery," *IEEE Trans. Geosci. Remote Sensing, vol. GE-30,* pp. 223-230, 1992.

[46] J.V. Martonchik, "Determination of aerosol optical depth and land surface directional reflectance using multiangle imagery," *J. Geophys. Res., vol. 102,* pp. 17015-17022, *1996*

[47] B.N. Holben, T.F. Eck, 1. Slutsker, D. Tanre, J.P. Buis, A. Setzer, E. Vermote, J.A. Reagan, and Y.J. Kaufman, "Multiband automatic sun and sky scanning radiometer system for measurements of aerosol," *Remote Sensing Environment,* (in press), 1997.

Table 1: Pure particle types in the ACP

Aerosol	r_1 (μm)	r_2 (μm)	r_c (μm)	σ	a	r_{eff} (μm)	n_r	n_i (band)	Vary with RH?	Shape
Sulfate/ nitrate 1 (Accum.)	0.007	0.7	0.2	1.86	n/a	0.38	1.53	0.0 (all)	Yes	Spheres
Sulfate/ nitrate 2 (Accum.)	0.05	2.0	0.45	1.30	n/a	0.53	1.43	0.0 (all)	No	Spheres
Mineral dust (Accum.)	0.05	2.0	0.47	2.60	n/a	0.53	1.53	0.0085(1) 0.0055(2) 0.0045(3) 0.0012(4)	No	Prolate/ oblate spheroids
Mineral dust (Coarse)	0.5	15.0	1.80	2.60		4.26				
Sea salt (Accum.)	0.05	1.0	0.35	2.51	n/a	0.62	1.50	0.0 (all)	Yes	Spheres
Sea salt (Coarse)	1.0	20.0	3.30	2.03		8.17				
Urban soot	0.001	0.5	0.012	2.00	n/a	0.036	1.75	0.455(1) 0.440(2) 0.435(3) 0.430(4)	No	Spheres
Biomass burning	0.007	2.0	0.13	1.80	n/a	0.31	1.43	0.0035 (all)	No	Spheres
Near-surface fog	0.5	50.0	n/a	n/a	2.5	18.50	1.33	0.0 (all)	No	Spheres
Thin cirrus	10.0	500.0	n/a	n/a	n/a	10.63	1.31	0.0 (all)	No	Fractal

Table 2: Tropospheric particle mixtures in the ACP

Conditions	Components	Minimum relative abundance	Maximum relative abundance
Clean maritime	Sulfate mode 1	1090	80%
	Sea salt accumulation	10%	80%
	Sea salt coarse	o%	*20%*
Industrial maritime	Sulfate mode 1	1 o%	*80%*
	Sea salt accumulation	10%	80%
	soot	o%	20%
Biomass burning maritime	Sulfate mode 1	1 o%	*70%*
	Sea salt accumulation	1 0 %	*70%*
	Biomass burning	20%	*80%*
Dusty maritime	Sulfate mode 1	1 0 %	*70%*
	Sea salt accumulation	10%	*70%*
	Mineral dust accumulation	20%	60%
Clean continental	Sulfate mode 1	10%	90%
	Mineral dust accumulation	10%	80%
	soot	0%	1 o%
ndustrial continental	Sulfate mode 1	1 o%	*90%*
	Mineral dust accumulation	0%	70%
	soot	20%	*40%*
Biomass burning continental	Sulfate mode 1	10%	*70%*
	Mineral dust accumulation	1090	70%
	Biomass burning	20%	80%
Dusty continental	Sulfate mode 1	1 o%	80%
	Mineral dust accumulation	10%	80%
	Mineral dust coarse	0%	20%

Table 3: Surface Type NDVI

Case	Surface Type	nadir NDVI no atmo.	extrap. NDVI no atmo.	extrap. NDVI τ_{aer} = 0.10	extrap. NDV1 τ_{aer} = 0.25	extrap. NDVI τ_{aer} = 0.50
1	Soil	0.088	0.089	0.122	0.133	0.128
2	Grassland	0.133	0.130	0.141	0.154	0.166
3	Steppe Grass	0.153	0.105	0.136	0.163	0.189
4	Hard Wheat	0.179	0.067	0.099	0.133	0.172
5	Irrigated Wheat	0.784	0.796	0.771	0.793	0.801
6	Hardwood forest	0.867	0.932	0.936	0.970	0,970
7	Pine Forest	0.782	0.862	0.864	0.893	0.872
8	Lawn Grass	0.763	0.777	0.750	0.772	0.775
9	Corn	0.520	0.439	0.464	0.508	0.539
10	Soybeans	0.896	0.946	0.949	0.981	1.000
11	Orchard Grass	0.555	0.511	0.534	0.576	0.589

Table 4: DDV aerosol retrieval results

$\theta_0 = 25°$		Sulfate RH 70% $r_{eff} = 0.21$	Sulfate] RH 90% $r_{eff} = 0.32$	Sulfate2 RH 0% $r_{eff} = 0.53$	Sea Salt (accum) RH 70% $r_{eff} = 0.70$	Sea Salt (accum) RH 90% $r_{eff} = 1.30$	Sea Salt (coarse) RH 70% $r_{eff} = 10.23$	Mineral Dust $r_{eff} = 0.53$	Mineral Dust $r_{eff} = 4.26$
Sulfate RH 70% $\tau = 0.10$	$\tau^{bestfit}$	.10 ± .07	.19 ± .09	.16 ± .14	.12 ± .13	.15 ± .28	.23 ± .17	.15 ± .09	.25 ± .25
	χ^2_{abs}	0.4	0.4	0.7	0.7	1.0	0.7	0.4	0.9
	χ^2_{geom}	0.4	0.4	1.8	3.8	I .9	9.5	0.2	0.8
	χ^2_{spec}	0.8	0.6	1.1	2.1	2.0	2.1	0.8	2.8
Sulfate RH 70% $\tau = 0.25$	$\tau^{bestfit}$	.25 ± .07	.43 ± .08	.33 ± .12	.23 ± .11	.32 ± .11	.35 ± .00	.32 ± .13	.00 ± .00
	χ^2_{abs}	0.3	0.2	1.2	1.4	2.0	1.5	0.9	7.6
	χ^2_{geom}	0.3	0.5	4.0	10	4.4	17	0.5	3.4
	χ^2_{spec}	0.7	0.4	2.1	7.7	5.5	5.3	14	5.7
Sulfate R 70% $\tau = 0.50$	$\tau^{bestfit}$	.48 ± .08	.77 ± .11	.68 ± .06	.40 ± .00	.70 ± .00	.50 ± .00	.86 ± .03	.00 ± .00
	χ^2_{abs}	0.2	0.3	2.2	11	10	24	4.6	67
	χ^2_{geom}	0.2	0.7	7.9	18	9.6	29	1.6	5.2
	χ^2_{spec}	0.7	0.8	49	6.8	82	13	148	4.3

Table 5: DDV aerosol retrieval results

$\theta_0 = \leq 5°$		Sulfate RH 70% $r_{eff} = 0.21$	Sulfate1 RH 90% $r_{eff} = 0.32$	Sulfate2 RH 0% $r_{eff} = 0.5$	Sea Salt (accum) RH 70%	Sea Salt (accum) RH 90% $r_{eff} = 1.30$	Sea Salt (coarse) RH 70%	Mineral Dust $r_{eff} = 0.53$	Mineral Dust $r_{eff} = 4.26$
Sulfate RH 70%	χ^2_{abs}	0.4	0.5	0.9	1.2	1.3	1.0	0.7	2.3
$\tau = 0.10$	χ^2_{geom}	1.8	2.0	4.2	5.9	6.7	18	2.4	7.6
	χ^2_{spec}	0.9	1.0	[illegible]	[illegible]	4.0	[illegible]	[illegible]	
Sulfate RH 70%	χ^2_{abs}	[illegible]		[illegible]	.27 ± .05	.42 ± .07	.25 ± .00	.36 ± .07	.00 ± .00
$\tau = 0.25$	χ^2_{geom}	0.3	0.5	2.0	2.7	3.2	10	2.3	36
	χ^2_{spec}	1.0	1.6	8.2	16	13	21	6.3	59
		0.8	1.6	22	[illegible]	71	14	320	5.1
Sulfate R 70%	χ^2_{abs}	[illegible]	[illegible]	[illegible]	.40 ± .00	[illegible].00	[illegible]	.80 ± .00	.00 ± .00
$\tau = 0.50$	χ^2_{geom}	0.2	0.6	9.3	46.	56	120	22	254
	χ^2_{spec}	1.4	[illegible]	22	25	24	287	36	102
		1.3	29	348	130	[illegible]	10	46	[illegible]

Table 6: DDV aerosol retrieval results

$\theta_0 = 65°$		Sulfate RH 70% $r_{eff} = 0.21$	Sulfate] RH 90% $r_{eff} = o.32$	Sulfate2 RH 0% $r_{eff} = 0.53$	Sea Salt (accum) RH 70% $r_{eff} = 0.70$	Sea Salt (accum) RH 90% $r_{eff} = 1.30$	Sea Salt (coarse) RH 70% $r_{eff} = 10.23$	Mineral Dust $r_{eff} = 0u53$	Mineral Dust $r_{eff} = 4.26$
Sulfate RH 70'% $\tau = 0.10$	$\tau^{bestfit}$	.1 0*.04	.14 ± .04	.15 ± .00	.10 ± .04	.15 ± .05	.15 ± .00	.14 ± .03	.31 ± .10
	χ^2_{abs}	0.4	0.7	2.0	2.4	1.7	2.4	1.6	5.8
	χ^2_{geom}	2.0	6.8	20	10	7.0	6.6	II	32
	χ^2_{spec}	0.9	3.3	1.2	4.9	7.6	11	60	546
Sulfate RH 70% $\tau = 0.25$	$\tau^{bestfit}$	.25 ± .04	.30± .04	.30 ± .00	.20 ± .00	.30 ± .00	.15* .00	.35 ± .00	.00 ± .00
	χ^2_{abs}	0.3	1.1	5.1	II	7.8	23	7.3	47
	χ^2_{geom}	1.8	6.4	26	93	45	87	52	73
	χ^2_{spec}	0.8	22	537	42	101	12	121	5.8
Sulfate R 70% $\tau = 0.50$	$\tau^{bestfit}$	.48 ± .06	.60 ± .00	.50 ± .00	.30 ± .00	.40 ± .00	.30 ± .00	.69 ± .04	.00 ± .00
	χ^2_{abs}	0. I	3.2	20	48.	49	72	43	! 49
	χ^2_{geom}	1.2	10	51	206	101	119	203	110
	χ^2_{spec}	0.6	304	2112	35	26	22	647	7.6

Table 8: EOF aerosol retrieval results

$\theta_0 = 25°$		Sulfate RH 70'70 $r_{eff} = 0.21$	Sulfate1 RH 90% $r_{eff} = 0.32$	Sulfate2 RH 0% $r_{eff} = 0.53$	Sea Salt (accum) RH 70% $r_{eff} = 0.70$	Sea Salt (accum) RH 90% $r_{eff} = 1.30$	Sea Salt (coarse) RH 70% $r_{eff} = 10.23$	Mineral Dust $r_{eff} = 0.53$	Mineral Dust $r_{eff} = 4.26$
Sulfate RH 70% $\tau = 0.10$	$\tau^{bestfit}$	.10 ± .04	.16 ± .05	.08 ± .05	.05 ± .05	.1 O*.O4	.04 ± .05	.16 ± .06	.24 ± .09
	χ^2_{hetero}	1.0 ± 0.8	1.1 ± 0.7	1.8 ± 1.4	4.3 ± 2.6	1.7 ± 0.9	11 ± 3.9	1.0 ± 0.9	2.0 ± 1.3
Sulfate RH 70% $\tau = 0.25$	$\tau^{bestfit}$	.25 ± .05	.38 ± .06	.22 ± .05	.12 ± .04	.28 ± .06	.09 ± .05	.40 ± .06	.36 ± .10
	χ^2_{hetero}	1.1 ± 0.8	1.5 ± 0.9	5.0 ± 1.9	14 ± 6	3.9 ± 2.0	48 ± 17	2,4 ± 1 .0	7.0 ± 3.8
Sulfate R 70% $\tau = 0.50$	$\tau^{bestfit}$	.51 ± .05	.73 ± .06	.54 ± .05	.25 ± .07	.70 ± .14	.21 ± .06	.73 ± .12	.60 ± .11
	χ^2_{hetero}	1.3 ± 0.9	5.0 ± 2.3	17 ± 7	48 ± 19	18 ± 7	196 ± 65	12 ± 5	64 ± 28

Table 7: Subimage Eigenvalues

1	2	3	4	5	6	7	8	9
5.84E-1	1.56E-1	5.25E-2	3.93 E-4	1.23 E-4	8.53 E-5	8.22E-5	6.98 E-5	6.40E-5

Table 9: EOF aerosol retrieval results

$\theta_0 = 45°$		Sulfate RH 70% $r_{eff} = 0.21$	Sulfate1 RH 90% $r_{eff} = 0.32$	Sulfate2 RH 0% $r_{eff} = 0.53$	Sea Salt (accum) RH 70% $r_{eff} = 0.70$	Sea Salt (accum) RH 90% $r_{eff} = 1.30$	Sea Salt (coarse) RH 70% $r_{eff} = 10.23$	Mineral Dust $r_{eff} = 0.53$	Mineral Dust $r_{eff} = 4.26$
Sulfate RH 70% $\tau = 0.10$	$\tau^{bestfit}$	.11 ± .04	.14 ± .05	.12 ± .05	.06 ± .06	.15 ± .04	.04 ± .05	.14 ± .04	.30 ± .09
	χ^2_{hetero}	1.4 ± 1.2	1.2 ± 0.9	2.6 ± 1.3	3.9 ± 2.0	3.7 ± 1.9	103 ± 45	2.1 ± 1.0	3. 9± 1.4
Sulfate RH 70% $\tau = 0.25$	τ^{bestfi}	.26 ± .03	.33 ± .04	.30 ± .06	.16 ± .07	.39 ± .09	.06 ± .04	.37 ± .07	.31± .11
	χ^2_{hetero}	1.0 ± 0.9	2.1 ± 1.0	8.9 ± 3.2	21 ± 12	17 ± 8	155 ± 66	8.7 ± 3.6	19 ± 8
Sulfate R 70% $\tau = 0.50$	τ^{bestfi}	.51 ± .04	.64 ± .04	.65 ± .13	.40 ± .08	.87 ± .16	.15 ± .06	.76 ± .15	.93 ± .19
	χ^2_{hetero}	1.6 ± 1.2	12 ± 5	68 ± 25	140 ± 67	49 ± 21	633 ±188	67 ± 29	322 ± 113

Table 10: EOF aerosol retrieval results

$\theta_0 = 65°$		Sulfate RH 70% $r_{eff} = 0.21$	Sulfate1 RH 90% $r_{eff} = 0.32$	Sulfate2 RH 0% $r_{eff} = 0.53$	Sea Salt (accum) RH 70% $r_{eff} = 0.70$	Sea Salt (accum) RH 90% $r_{eff} = 1.30$	Sea Salt (coarse) RH 70% $r_{eff} = 10.23$	Mineral Dust $r_{eff} = 0.53$	Mineral Dust $r_{eff} = 4.26$
Sulfate RH 70% $\tau = 0.10$	$\tau^{bestfit}$	.10 ± .06	.10 ± .07	.09 ± .06	.08 ± .06	.11 ± .04	.06 ± .06	.10 ± .05	.21 ± .08
	χ^2_{hetero}	2.4 ± 1.3	5.3 ± 1.7	23 ± 9	25 ± 12	23 ± 12	114 ± 39	19 ± 9	20 ± 11
Sulfate RH 70% $\tau = 0.25$	τ^{bestfi}	.25 ± .05	.24 ± .06	.23 ± .08	.21 ± .07	.28 ± .06	.15 ± .05	.27 ± .07	.39± .11
	χ^2_{hetero}	1.3 ± 1.0	17 ± 7	92 ± 43	55 ± 26	46 ± 19	440 ±165	57± 27	52 ± 21
Sulfate R 70% $\tau = 0.50$	τ^{bestfi}	.51 ± .04	.47 ± .05	.43 ± .04	.42 ± .08	.54 ± .06	.28 ± .09	.54 ± .07	1.15 ±.14
	χ^2_{hetero}	1.9± 1.1	125 ± 53	275 ± 93	189 ± 86	114 ± 51	620 ± 278	751 ± 251	779 ±180

FIGURE CAPTIONS

Figure 1. Summary of MISR aerosol retrieval techniques.

DARK WATER	DENSE DARK VEGETATION	HETEROGENEOUS LAND
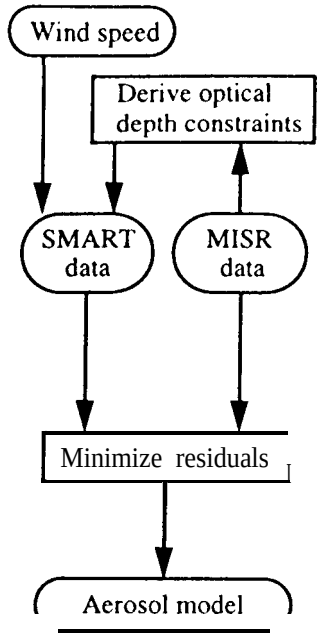	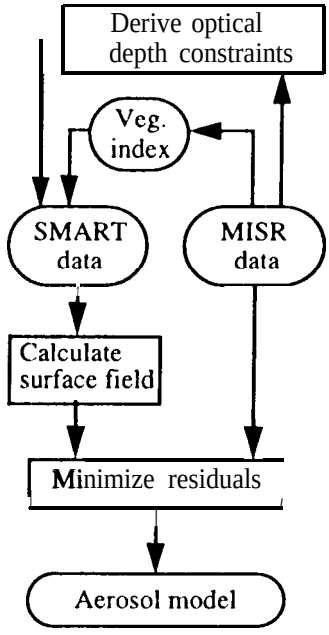	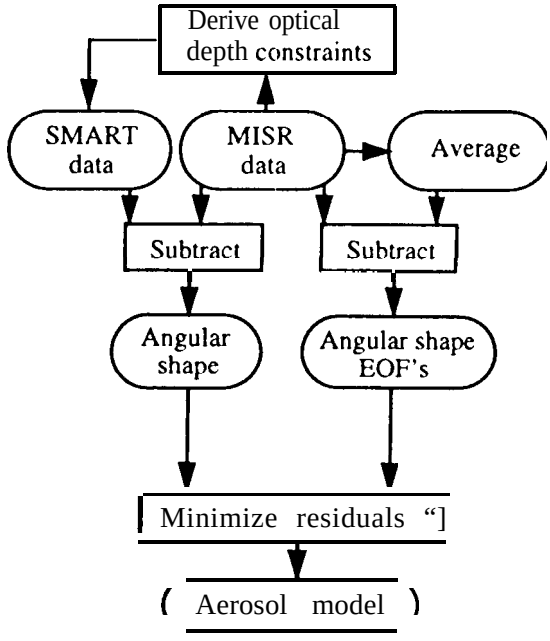
Uses MISR 672, 866 nm bands. Requires wind speed to establish glitter and whitecap reflectance.	Uses MISR 446,672 nm bands. Requires use of standard DDV bidirectional reflectance model.	Uses all MISR bands. Does not require surface bidirectional reflectance or albedo assumptions, but surface must have spatial contrasts.

Figure 1

AUTHOR BIOGRAPHIES

John V. Martonchik received the B.S. degree in physics from Case Institute of Technology in 1964 and the Ph.D. degree in astronomy from the University of Texas at Austin in 1974. He joined JPL in 1972 and currently holds the position of Research Scientist. His experiences include telescopic and spacecraft observations of planetary atmospheres, laboratory and theoretical studies of the optical properties of gaseous, liquid, and solid materials, and development and implementation of one- and three-dimensional radiative transfer and line-by-line spectroscopy algorithms for studies of planetary atmospheres and Earth tropospheric remote sensing. He has been a Co-Investigator in several NASA programs and is the Algorithm Scientist for aerosol and surface retrievals on MISR.

David J. Diner received the B.S. degree in physics with honors from the State University of New York at Stony Brook in 1973 and the M.S. and Ph.D. degrees in planetary science from the California Institute of Technology in 1977 and 1978, respectively. He has been at the Jet Propulsion Laboratory since 1978, first as a National Research Council Resident Research Associate, then as a contractor with Ball Aerospace, and since 1981 as a JPL employee. He is currently a Member of the Technical Staff and Leader of the Multi-angle Imaging Science Element in the Earth and Space Sciences Division. He has been involved in numerous NASA planetary and Earth remote-sensing investigations, and is presently Principal Investigator of the EOS Multi-angle Imaging SpectroRadiometer (MISR) experiment and its airborne counterpart, AirMISR.

Ralph A. Kahn received his Ph.D. in applied physics from Harvard University in 1980, concentrating in atmospheric physics and radiative transfer. His research interests include the climate and climate history of Mars, Venus, and Earth. A primary theme of his work has been to analyze global-scale data sets, bringing to bear theoretical models and other observations as needed. He was an experimenter on the Viking Lander Imaging team, and was responsible for imaging the sunset of Mars. He has been a Research Scientist at the Jet Propulsion Laboratory since 1988, where he works primarily on Earth observations. He is a member of the MISR science team, specializing in tropospheric aerosol research. Dr. Kahn has lectured on global change and atmospheric physics at UCLA, the Claremont Colleges, and Caltech, and is editor and founder of PUMAS, the on-line journal of science and math examples for pre-college education (http://

pumas.jpl.nasa.gov).

Thomas P. Ackerman received the M. SC. degree in physics in 1971 and the Ph. D. in atmospheric science in 1976 from [he University of Washington. He has been a member of the faculty at the Pennsylvania State University since 1988 and holds the positions of Professor of Meteorology and Associate Director of the Earth System Science Center. Prior to 1988, he was a research scientist at the NASA Ames Research Center. His research interests include radiative transfer in planetary atmospheres, the effect of aerosol and clouds on the Earth radiation budget, and remote sensing of aerosol and cloud properties both from ground and satellite. He is currently a member of the MISR science team and Site Scientist for the Tropical Western Pacific site in the DOE Atmospheric Radiation Measurement Program.

Michel M. Verstraete received his License en Physique (1974) from the Université Catholique de Louvain in Louvain-la-Nueve, Belgium, his License Spéciale en Géophysique (1976) from the Université Libre de Bruxelles, Belgium, and both his M. SC. in Meteorology (1978) and D. SC. in Atmospheric Sciences (1985) from the Massachusetts Institute of Technology in Cambridge, MA. He worked for the World Meteorological Organization in Geneva, Switzerland and Nairobi, Kenya from 1979-1981, at the National Center for Atmospheric Research (NCAR) in Boulder, CO from 1982-1989, taught at the University of Michigan in Ann Arbor from 1989-1990, and is currently employed at the Space Applications Institute (SAI) in Ispra, Italy. He is a member of various scientific advisory committees of the European Space Agency (e.g., MERIS) and is a MISR science team member. His initial work on topics such as the modeling of atmosphere-biosphere interactions and desertification led him to his current interest in the quantitative exploitation of satellite remote sensing data for the detection and characterization of terrestrial surface properties.

Bernard Pinty received his Maîtrise de Chimie and DEA (1977), thèse de troisième cycle en Physique de I'Atmosphere (1980) and thèse d'Etat (1988) from the Université Blaise Pascal in Clermont-Ferrand, France. He is presently affiliated with the Space Applications Institute (SAI) in Ispra, Italy. He visited the National Center for Atmospheric Research (NCAR) in Boulder, CO (1988- 1989), served as Deputy Director of the Laboratoire d'Etudes et de Recherches en Télédétection Spatiale (LERTS) in Toulouse, France (1990- 1992), and was professor of phYsics at [he University Blaise Pascal, France (1993- 1996). Dr. Pinty received the Zel'dovich medal from

COSPAR (1990) and is **a member** of the MERIS Scientific Advisory Group of the European Space Agency and a MISR science team member. He serves as an Associate Editor for the Journal of Geophysical Research-Atmosphere. His main interests include research on the theory of radiation transfer in plant canopies and, more generally, the development of tools to quantitatively interpret satellite remote sensing data in the solar spectral domain.

Howard R. Gordon is Professor of Physics at the University of Miami. He received the B.S. degree in physics from Clarkson College of Technology (now Clarkson University) in 1961 and the M.S. and Ph.D. degrees in physics from the Pennsylvania State University in 1963 and 1965, respectively. In 1975 he became a member of the Nimbus-7 Coastal Zone Color Scanner (CZCS) experiment team --- the first satellite instrument designed to study the variability in the distribution of phytoplankton in the ocean. He was awarded the Public Service Medal by NASA in 1982 for the development of methods for recovering phytoplankton pigment concentrations from CZCS imagery. He is presently a science team member of a number of new satellite instruments designed for a long-term assessment of global climate: the Sea-viewing Wide-Field-of-View Sensor (SeaWiFS), a CZCS follow-on to globally monitor the concentration of marine phytoplankton, launched August 1, 1997; the Moderate Resolution Imaging Spectroradiometer (MODIS) to be launched in 1998; and the Multi-angle Imaging SpectroRadiometer (MISR) to be launched in 1998. He was elected Fellow of the Optical Society of America in 1977, and has served as the Oceanic Optics Topical Editor of Applied Optics.